Multi-spectral observations of flares

F. Zuccarello⋆

Dipartimento di Fisica e Astronomia, Sezione Astrofisica, Via S. Sofia 78, 95125 Catania, Italy

Received XXXX, accepted XXXX
Published online XXXX

Key words Solar flares, solar atmosphere, magnetic reconnection, high-resolution observations.

Observations show that during solar flares radiation can be emitted across the entire electromagnetic spectrum, spanning from gamma rays to radio waves. These emissions, related to the conversion of magnetic energy into other forms of energy (kinetic, thermal, waves) through magnetic reconnection, are due to different physical processes that can occur in different layers of the Sun. This means that flare observations need to be carried out using instruments operating in different wave-bands in order to achieve a complete scenario of the processes going on. Taking into account that most of the radiative energy is emitted at optical and UV wavelengths, observations carried out from space, need to be complemented by observations carried out from ground-based telescopes. Nowadays, the possibility to carry on high temporal, spatial and spectral resolution from ground-based telescopes in coordinated campaigns with space-borne instruments (like, i.e., IRIS and HINODE) gives the opportunity to investigate the details of the flare emission at different wavelengths and can provide useful hints to understand these phenomena and compare observations with models. However, it is undoubted that sometimes the pointing to the flaring region is not an easy task, due to the necessity to provide the target coordinated to satellites with some hours in advance. Some problems arising from this issue will be discussed. Moreover, new projects related to flare catalogues and archives will be presented.

1 Introduction

The electromagnetic radiation emitted during solar flares can span from γ rays at 100 MeV to decameter radio waves. Several mechanisms are responsible for emission on such a broad interval. The γ - ray lines emitted by heavy ions are excited by protons in the MeV range (Chupp 1973). The hard X-ray ($\geq$ 10 keV) are emitted due to bremsstrahlung from electrons experiencing Coulomb collisions, and the spectrum they give rise can be approximated by a power-law, showing a non-thermal shape. This emission is generally observed in locations approximately coinciding with the loops (or arcade) footpoints and with a source located above the flare loop top. The soft X-ray emission, observed since the pre-flare phase, shows a thermal spectrum and, together with millimeter and EUV (extreme ultraviolet) emissions, give indication on the fact that the plasma filling the post-flare loops reaches temperatures of 1.5 to 30 MK.

The flare emission at optical wavelengths, like for instance in the H_α line, or in some cases, in white light (WL), starts to increase during the impulsive phase of the flare and is due to the response of the chromospheric and photospheric plasma to accelerated particles colliding with the lower atmospheric layers and heating them (see, e.g., Fletcher et al. 2011).

Broadband radio emissions in the range 1 - 100 GHz are due to free-free emission and to gyro-synchrotron emission from mildly relativistic electrons gyrating along the loop field lines (see, e.g. Benz 2008, for a review and references therein).

All these processes give rise to the well-known flare signatures, like a pair of bright ribbons in H_α (sometimes, white light: WL) and UV/EUV images (see, e.g., Fig. 1), and loop brightness increase in the EUV and soft X-ray ranges. The ribbons, located parallel to the magnetic inversion line, move away one another with an initial velocity of $\sim$ 100 km s^{-1}, decreasing to less than 1 km s^{-1} over some hours. During this phase, in the EUV lines and in the X-ray range it is possible to detect a system of post-flare loops initially appearing at low altitudes and subsequently moving upward in the corona (Aschwanden 2004; Benz 2008).

Most of the flare events showing these features are characterized by the eruption of a filament that was initially located along the magnetic neutral line: in the standard model of solar flares, the eruption of the filament represents the initial driver of the flare and its rise toward higher atmospheric layers is accompanied by the formation of an X-type neutral point, a current sheet and the breakage and reconnection of magnetic field lines. Due to the filament rise, there is also a continuous rise of the reconnection point, so that the newly reconnected field lines beneath the X-type neutral point have an increasingly larger height and wider footpoint separation (the standard model is also called CSHKP 2D magnetic reconnection model, after the name of Carmichael (1964), Sturrock (1996), Hirajama (1974) and Kopp & Pneuman (1976)).

More in general, the flare phenomenon is now interpreted in the framework of theories assuming that the main

⋆ Corresponding author: e-mail: fzu@oact.inaf.it

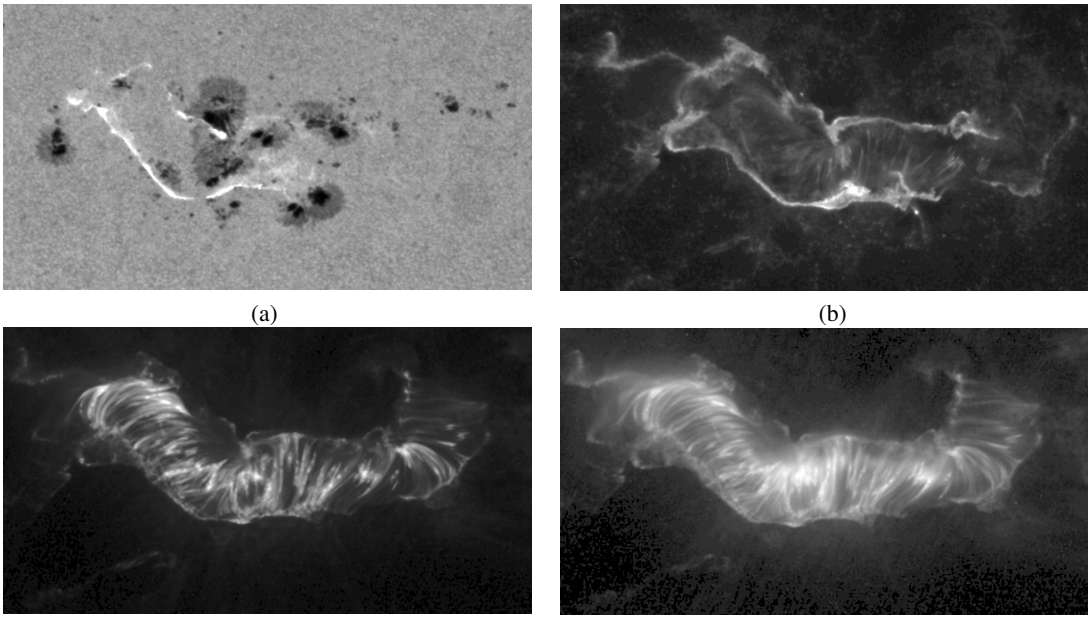

Fig. 1 Multi-wavelength TRACE observations of the Bastille day flare occurred in AR NOAA 9077 on 2000 July 14. (a): WL image acquired at 10:28 UT; (b) 1600 Å image acquired at 10:48:24 UT; (c) 195 Å image taken at 10:48:38 UT; (d) 171 Å image acquired at 10:48:32 UT.

process at their base is magnetic reconnection (Forbes & Priest 1995), occurring when a catastrophic loss of mechanical equilibrium sets in.

In the reconnection region the magnetic energy is converted into heating of the local coronal plasma, acceleration of non-thermal particles and slow MHD shocks. The thermal conduction fronts, the accelerated particles and the shocks contribute to the heating of the chromospheric footpoints of newly reconnected field lines. Consequently, due to the chromospheric plasma overpressure, the plasma evaporates and fills the post-flare loops, which become observable at EUV and soft X-ray ranges.

When reconnection occurs above the top of a magnetic loop (more specifically, at the extremity of a magnetic cusp), the coronal source detected in hard X-ray can be considered as an intermediate thin-thick target (thick target for electrons with lower energy, thin target otherwise) (Benz 2008). Those electrons, characterized by higher energies, that are not stopped at this location, precipitate along the magnetic field lines toward the lower atmospheric layers and when they hit the chromosphere, they meet a sort of second target (here a thick-target), heat the plasma, then chromospheric evaporation takes place, and ribbons and post-flare loops are observed. As a consequence, studies on the evaporation / condensation process, leading to the determination of plasma velocities and to the temperature of the ribbons observed at various wavelengths are of primary importance.

On the other hand, it is also important to determine what are the conditions that lead to the catastrophic loss of equilibrium of the magnetic field. Starting from the obvious consideration that the more complex is the magnetic field configuration, the higher is the probability that this loss of equilibrium takes place, one parameter that is often used to have hints on the magnetic field out of potentiality state, is the magnetic helicity, which increases due to magnetic flux emergence and/or shearing and twisting of the photospheric footpoints. In the same context, i.e., the magnetic field configuration, an important role is played by the so-called δ-spots, which are sunspots characterized by umbrae of opposite polarities in the same penumbra. These δ-spots in fact seem to be one of the preferred sites of most flares and the investigation of this kind of features and of the conditions leading to flare triggering has recently benefitted by high resolution observations.

From the scenario depicted above, it is clear that observations of flares must be carried out in several electromagnetic ranges and therefore both ground-based and space-based datasets are necessary in order to improve our knowledge on the physical parameters (temperature, density, emission measure, differential emission measure, plasma velocity, accumulated magnetic helicity, total electron flux, electron spectral index, low energy cut-off, etc.) that characterize the flare scenario, allowing us to verify the consistency of and eventually to improve the standard flare model.

In this scenario, the new possibilities offered by high-resolution ground-based observations, as well as by most recent satellite instruments, are expected to better clarify the processes cited above, providing most stringent ranges for several parameters characterizing the several stages and interplay of the complex flare phenomenon.

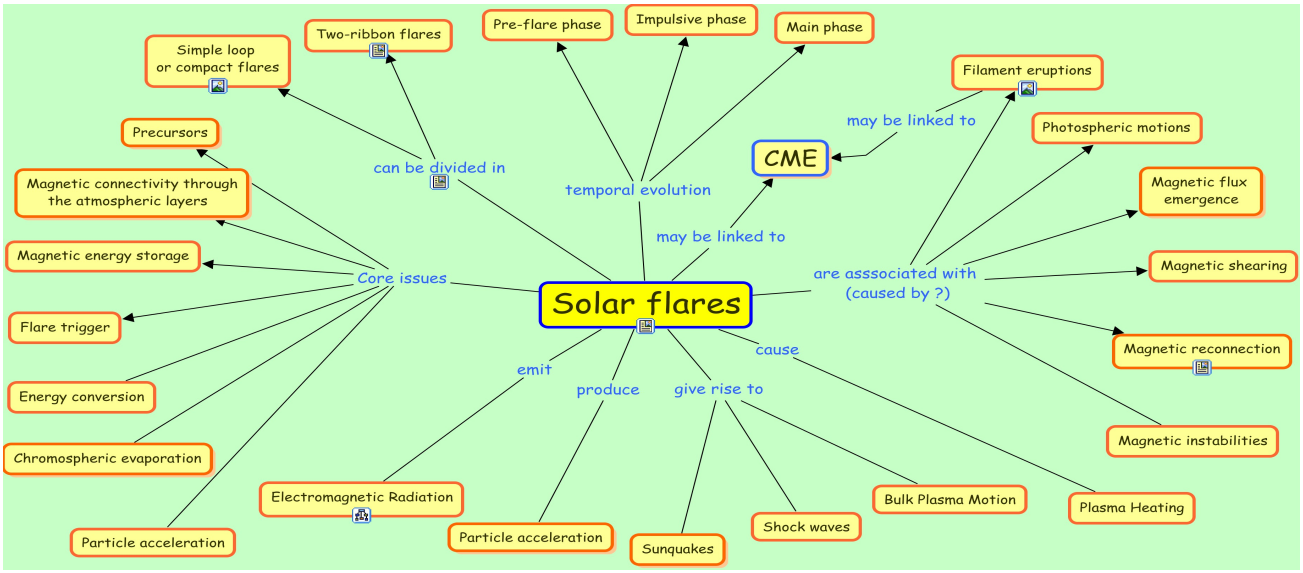

Fig. 2 Conceptual map describing the complexity of the flare phenomenon and the interplay among several atmospheric layers and physical processes.

2 Flare overview and multi-spectral observations

In the previous Section the complexity of the flare phenomenon has been briefly summarized. In this regard, in order to provide a *quick-look* description of the different morphological, evolutionary and physical characteristics of solar flares, we refer to the conceptual map reported in Fig. 2, where, besides than the main morphological classification and temporal phases, we can distinguish between the phenomena that are associated to flares and those that are produced by flares. The conceptual map also shows (on the left side) a list of the still unclear processes occurring during these phenomena that represent the core issues of the research on these highly energetic events (we recall that the energy involved is in the range 10^{28} - 10^{32} erg).

In particular, when considering the temporal evolution of solar flares, we can distinguish between three main phases: a pre-flare, an impulsive and a main (or gradual) phase.

During the pre-flare phase, it is possible to detect an increase of emission in the X-soft (line broadening seen $\sim$ 10 minutes prior to HXR (hard X-rays) onset) and EUV (brightening seen between 1 - 40 minutes prior to HXR onset) ranges, while several phenomena, like filament activation and blue shifted events in the H_α line are observed in the chromosphere.

The impulsive phase is the phase of rapid energy release, characterized by *impulsive* or spiky emission in the EUV and UV ranges, and often a close temporal relationship between UV and HXR emission can be observed; during the same phase impulsive SXR (soft X-rays), HXR and microwave bursts can be detected, as well as large upflows in SXR. The HXR and microwave bursts are often characterized by double source structures, providing information on the energy release site in the corona. Moreover, it is during the impulsive phase that it is possible to observe γ-ray continua and lines.

During the gradual phase, H_α and (sometimes) WL emission in separating bright ribbons are observed (see Fig. 3, *left*), while the EUV emission is mainly concentrated in post-flare loops and kernels (see Fig. 3, *right)*. Strong SXR emission, rising SXR loops and HXR sources are also observed.

In Table 1 we report the effects or phenomena that can be observed at different spectral ranges in relation to flare occurrence. We also stress that recently, high resolution spectro-polarimetric observations have provided useful information on the magnetic field configuration in the photosphere, allowing for instance, through force-free field extrapolations, a comparison between the pre- and post-flare configuration, or the determination of the magnetic helicity, which provides indication on the emergence of new magnetic flux or on the degree of twisting and/or shearing of the magnetic field lines (see, i.e., Romano & Zuccarello 2011).

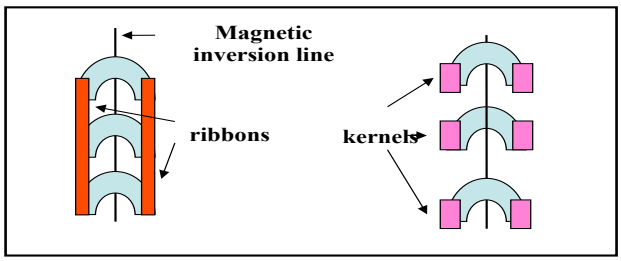

Fig. 3 Schematic configuration of a two-ribbon flare. *Left*: the ribbons, parallel to the magnetic inversion line, are indicated by red rectangles and correspond to the footpoints of a magnetic arcade; *right*: bright kernels, at the location of some loop footpoints, are shown.

Table 1 Observations at different wavelength ranges

Spectral range or line	Effects and/or Observables
WL	active region (AR) morphology in photosphere
	precursors (magnetic flux emergence, sunspots motions, shearing velocity fields, etc.)
	signatures of WL ribbons and kernels
	changes in sunspots penumbrae after the flare
	relation to CME occurrence (from coronograph observations)
Hα	AR morphology in chromosphere
	filament activation and rise
	Hα ribbons or kernels (morphology, separation, fine structure)
	post-flare Hα loops
	changes in line profiles (input for comparisons with models))
	plasma diagnostics (temperature, density, velocity)
UV/EUV	AR morphology in chromosphere - transition region - corona
	plasma evaporation/condensation
	post-flare loops (timing, spatial configuration, correlation with WL/Hα ribbons)
	fine structure of erupting filaments (flux ropes)
	plasma diagnostics (temperature, density, emission measure, velocity)
X-rays	sigmoidal shape of coronal arcades
	increased soft X-ray emission in coronal loops
	impulsive brightening in soft X-rays
	rising of SXR loops
	Hard X-ray sources - correlation with brightenings in the other bands
	Hard X-ray spectrum: input for models (i.e. Radyn, Flarix)
Radio	thermal and non-thermal emission
	gyro-synchrotron from high energy electrons
	bremsstrahlung radiation

Moreover, using some inversion codes, like SIR (Ruiz Cobo & del Toro Iniesta 1992) it is also possible to derive from spectro-polarimetric data, besides than several magnetic properties, also temperature maps of the region involved by flares.

3 Some case studies

In the following we describe some case studies, in order to provide some examples of the different information and/or parameters that can be obtained when comparing observations acquired in different wavelength ranges. In particular, we will describe the results obtained from the analysis of flares observed by different ground-based and satellite instruments.

3.1 SOL20031028: domino effect

This flare occurred in AR NOAA 10486 on 2003 October 28 and was analyzed using data acquired by INAF-Catania Astrophysical Observatory (INAF-OACT; Zuccarello, Contarino & Romano, 2011), the Michelson Doppler Imager (MDI; Scherrer et al. 1995) on board the SOlar and Heliospheric Observatory (SOHO; Domingo et al. 1995), the Transition Region And Coronal Explorer (TRACE; Handy et al. 1999), the Reuven Ramaty High Energy Solar Spectroscopic Imager satellite (RHESSI, Lin et al. 2002), the Ondrejov Radiospectrometer (Jiricka et al. 1993).

Comparing the multi-wavelength data and the magnetic field configuration inferred from linear force-free field extrapolations it was possible to conclude that the active region was characterized by a multipolar magnetic field configuration (see Fig. 4, *left*). Moreover, the Hα observations showed the consecutive activation and/or eruption of three filaments, while in the EUV range several brightening during the pre-flare and impulsive phases, in sites corresponding to separatrix surfaces, were observed. TRACE coronal images showed post-flare loops that were observed almost simultaneously in distant arcades (see Fig. 4, *right*).

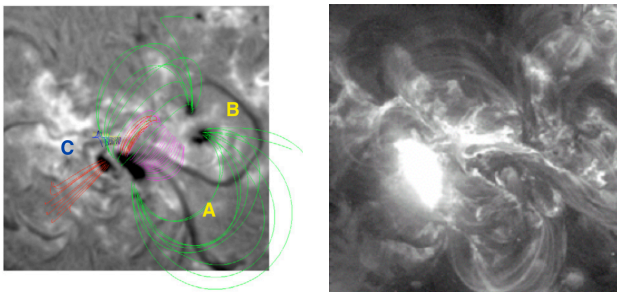

Fig. 4 SOL20031028. *Left*: Hα image showing the presence in chromosphere of three filaments, named A, B and C, that were destabilized or erupted sequentially as a consequence of the *domino effect* (see text). The magnetic field lines inferred from a linear force-free field extrapolation are shown with different colors; *Right*: TRACE 171 Å image showing the coronal arcades involved in the X17.2 flare (adapted from Zuccarello et al. 2009).

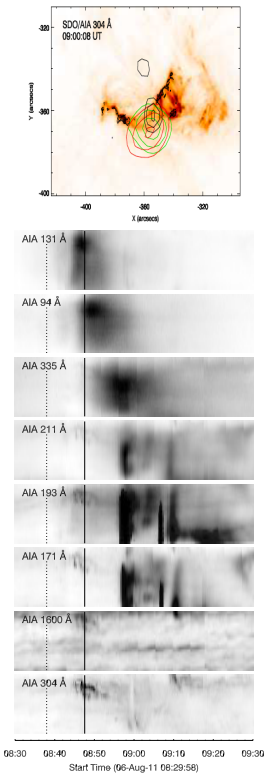

Fig. 5 SOL20110806. *top*: SDO/AIA 304 Å image acquired at around 09:00 UT (reverse intensity scale), with overplotted RHESSI emission contours from simultaneous observations: 3-6 keV (red), 6-12 keV (green), and 25-50 keV (black). The black contours represent the SST Ca II H emission. The *extruding structure* is the region between -400 and -300 [x-coordinate] and -360 [y-coordinate]; *bottom*: SDO/AIA intensity time slices along the extruding structure for different wavelengths. The bottom of each panel corresponds to the easternmost part of the extruding structure, the top to the part closest to the δ-spot. The dotted vertical lines indicate the start of the flare according to the HXR emission; the solid vertical lines, the flare peak (adapted from Guglielmino et al. 2016)

This flare was interpreted in terms of a *domino effect*, characterized by successive destabilizations of the magnetic field: initially filament A erupted and this caused the lift-off of the inner arcade (magenta lines in Fig. 4, *left*). Reconnection at null points located in the lower atmosphere took place, producing a decrease of tension in the higher (green) arcade. As a result, filaments B and C were not confined anymore by these field lines and started to rise, triggering the X17.2 flare (Zuccarello et al. 2009).

3.2 SOL20110806: flare in a δ-spot

This flare occurred in AR NOAA 11267 on 2011 August 8 and was analyzed using data acquired by the CRisp Imaging Spectropolarimeter (CRISP; Scharmer et al. 2008) mounted at the Swedish Solar Telescope (SST; Scharmer et al. 2003), the Helioseismic and Magnetic Imager (HMI; Scherrer et al. 2012) and the Atmospheric Imaging Assembly (AIA;

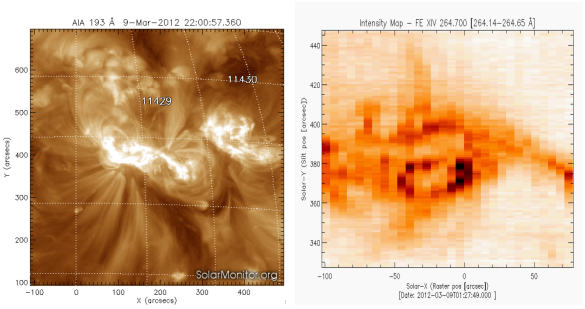

Fig. 6 SOL20120309. *Left*: AIA/SDO 193 Å image of AR NOAA 11429 acquired at 22:00:57 UT, showing the coronal configuration of the active region; *right*: EIS/HINODE intensity map acquired in the line Fe XIV 264.700 Å (reverse color) during the flare occurrence. The brightest pixels indicate the location of the footpoints.

Lemen et al. 2012) onboard the Solar Dynamics Observatory (SDO, Pesnell et al. 2012), the X-ray Telescope (XRT, Golub et al. 2007) aboard the Hinode satellite (Kosugi et al. 2007), and the RHESSI satellite.

The flare, of GOES class C4.1, was initiated along the neutral line of a δ-spot. The bulk of the X-ray emission took place in the δ-spot region, where the plasma heated up to 2×10^7 K. During the gradual phase, the AIA/SDO images showed the development of a Y-shaped structure in the corona and in the high chromosphere, with an extruding structure directed from the emitting region above the preceding δ-spot toward the following sunspot (see Fig. 5, *top*). This structure cooled down in a few tens of minutes and moved along a direction which was opposite to the flare ribbon expansion in the δ-spot area. The extruding structure was first observed in the hottest AIA lines, while in the 211, 193, 171 Å lines had a peak simultaneous to a dimming in the 304 Å line at 09:00 UT (see Fig. 5, *bottom*). The analysis of the data acquired by the RHESSI satellite showed that the X-ray emission was localized in the region close to the crossing point of the coronal Y-shaped structure. This event was interpreted as a manifestation of magnetic reconnection, probably due to an asymmetric magnetic configuration in a highly sheared region (Guglielmino et al., 2016).

3.3 SOL20120309: chromospheric evaporation

This flare of GOES class C4.7 occurred in AR NOAA 11429 on 2012 March 9 and was analyzed using data acquired by AIA/SDO and EIS/HINODE instruments. Aim of this analysis was to determine the local plasma dynamics (flows) and density as a function of space and time.

High resolution EUV spectroscopic data acquired by EIS over two footpoints of the C4.7 flare were used to determine these parameters, while AIA/SDO images were used to determine the location of flare ribbons/kernels (see Fig. 6).

The analysis carried out using the Fe XXIII 263 Å line (10 MK) showed a blue asymmetry (~ 90 km s^{-1}) at one of the flare kernel/footpoint, indicating chromospheric evaporation (spectral signatures of chromospheric evaporation

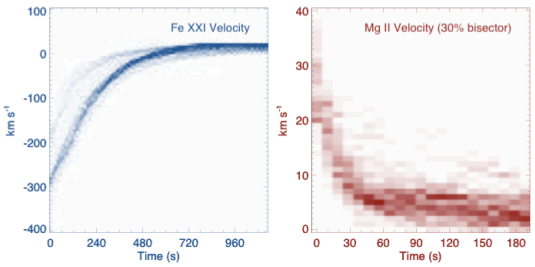

Fig. 7 SOL20140910. *Left*: line of sight plasma velocity as a function of time obtained from the analysis of the Fe XXI line: the negative values indicate upflows during the evaporation process; *right*: downflows inferred from the analysis of the Mg II line, showing the temporal evolution of the condensation process (note the different time ranges) (adapted from Graham and Cauzzi, 2015).

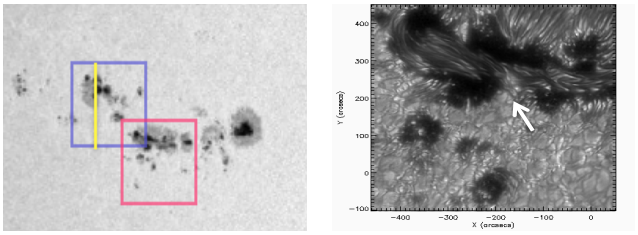

Fig. 8 SOL20141107. *Left*: HMI/SDO continuum image acquired at 15:58:12 UT, showing the photospheric configuration of NOAA 12205 on November 7, 2014; the blue and red boxes indicate two fields of view used to acquire data with the ROSA instrument, while the yellow line indicates the IRIS slit position; *right*: ROSA G-band image showing a portion of the sunspots involved by the X1.6 flare. The white arrow indicates the location of the WL ribbon (see text).

are velocity blueshift in high temperature emission lines). Moreover, the ratio Fe XIV (λ 264 Å)/(λ 274 Å) (2 MK) was used as a density diagnostic, allowing to conclude that the density of the upflowing plasma increased by more than one order of magnitude from the pre-flare average density value ($\sim 5 \times 10^9$ cm^{-3}) (Polito et al. 2014).

3.4 SOL20140910: evaporation and condensation

This X1.6 flare occurred in AR NOAA 12158 on 2014 September 10 and was analyzed using data acquired by the Interface Region Imaging Spectrograph (IRIS; De Pontieu et al. 2014) and the AIA/SDO instrument.

The presence of contemporary evaporation and condensation processes was evidenced: using the IRIS data acquired in the Fe XXI line (10 MK), upflows were detected in 80 pixels along one ribbon moving along the IRIS spectrometer slit, while in the Mg II line, the results indicate plasma downflows during a shorter timescale. In particular, following the evolution of the flare ribbon, each activation of a new footpoint displayed the same initial coronal upflows of up to $\sim$ -300 km s^{-1}, and chromospheric downflows up to 40 km s^{-1} (see Fig. 7). The authors concluded that, although the coronal flows could be delayed by over 1 minute with respect to those in the chromosphere, the temporal evolution of flows was quite similar between all pixels, and consistent with predictions from hydrodynamic flare models (Graham & Cauzzi, 2015).

3.5 SOL20141107: ribbon in the G-band

On 7 November 2014, during a coordinated observing campaign involving both ground-based instruments: the Rapid Oscillations in the Solar Atmosphere (ROSA; Jess et al. 2010) operating at the NSO/Dunn Solar Telescope (DST) and satellite instruments (IRIS, AIA/SDO, HMI/SDO and GOES), two flares were observed in NOAA 12205. The first flare, of GOES class C7.0, started at 16:10 UT, with peak at 16:39 UT and ended at 16:45 UT; the second flare, of class X1.6, started at 16:53 UT, peaked at 17:26 UT and ended at 17:34 UT.

Fig. 8 (*left*) shows the photospheric configuration of the AR; the two boxes indicate the different fields of view observed by ROSA, while the yellow line indicates the IRIS slit position during the observations. From a preliminary analysis of the ROSA dataset, it has been possible to detect signatures of emission in the G-band during the X1.6 flare (see Fig. 8, *right*), indicating the presence of a ribbon moving with a velocity of $\sim$ 10 - 15 km s^{-1}. An in-depth study has been carried out in order to determine the optical depth of the ribbon (Prochazka et al. 2016).

4 Catalogues and archives

Several flare catalogues based on space observations are available on-line, as listed in Table 2 and at the link:
http://www.ssl.berkeley.edu/ moka/rhessi/catalogs.html.
In these catalogues, many information about the flares are provided, such as the times of beginning, peak, end, the GOES class, the active region which originated them, etc.

Recently, a new catalogue is available to the scientific community (https://star.pst.qub.ac.uk/wiki/doku.php/public /solarflares/start), which provides also information on events that have been observed using ground-based facilities, such as the DST, the SST, the Ondrejov Telescopes, the Big Bear Solar Observatory, the INAF-OACT, the Nobeyama Radioheliograph, the Télescope Héliographique pour l'Étude du Magnétisme et des Instabilités Solaires (THEMIS; Arnaud et al. 1998), the Large Coronagraph and Multi-Channel Subtractive Double Pass Spectrograph of the Astronomical Institute of the University of Wroclaw, the Kanzelhohe Observatory, the Horizontal Telescope and the MSDP spectrograph telescopes .

This catalogue has been prepared by the F-CHROMA consortium (http://www.fchroma.org) and its final aim is to provide the scientific community with flare dataset including both ground-based and satellite observations of a selected number of events.

Table 2 Catalogues or Lists of flares observed by satellites

Satellite/instrument	Type(*)	Period covered
Yohkoh	C	1991 - 2001
TRACE	C	1998 - 2009
RHESSI	L	2002 - present
Hinode	C	2006 - present
Hinode/XRT	C	2006 - present
Hinode/EIS	C	2006 - present
SOHO/EUVI	C	2006 - present
FERMI/GBM	L	2008 - present

(*) C = catalogue, L = list

5 Discussion and Conclusions

In this paper we have summarized some of the main characteristics of flares, taking into account the importance of carrying out the observations in different spectral ranges, due to the different temporal evolution of these phenomena in each wavelength band, but also because different physical processes can be studied in each spectral range.

We stressed also the importance of performing coordinated observing campaigns between ground-based and space-based instruments, due to the necessity to integrate the optical and radio dataset with others acquired in other bands (UV, EUV, X, γ), in order to get a more complete scenario of the processes going on.

In this regard, it is worthwhile to stress that concerning the procedure of the target selection, often some issues can arise : for organizational reasons, the coordinates of the target must be provided in advance (from some hours to 1 - 2 days) to the satellite instrument planner and in most of the cases the flare takes place outside the selected field of view. So, we might have timely and spatially accurate ground-based observations, while the satellite datasets only provide context information, which are of course very useful, but not really spatially related to the exact flaring region.

This is one of the reasons why for the moment we have very few high resolution dataset covering contemporarily different spectral bands.

We provided some examples of flares that were studied using dataset acquired at different wavebands. These examples concerned the occurrence of a so-called domino effect that caused a sequence of phenomena taking place in different atmospheric layers, whose global scenario was possible to evaluate thanks to these multiple observational modes. We also showed how the different brightening timing could be evidenced in the development of a Y-shaped flare occurred in a δ-spot, as well as some examples of evaporation and condensation in flaring sites, again evidenced by multi-wavelength observations.

It is therefore important to continue and improve this modality of observation in order to be able to provide an answer to several questions that are still under debate: what are the rate and the location of the reconnection, how reconnection can convert part of the energy into non-thermal particles, what are the mechanisms of interaction between the particles and the ambient plasma, just to cite a few.

In summary, if we want to obtain realistic models of solar flares, we must take into account:

- the emission in different wavelengths and its time evolution
- what physical processes might give rise to such emissions
- the involvement of several atmospheric layers and the timeline of this involvement
- the possibilities offered by comparing high-resolution ground-based solar data with satellite data.

Acknowledgements. The research leading to these results has received funding from the European Commission's Seventh Framework Programme under the grant agreements F-CHROMA (project no 606862) and SOLARNET (project no 312495). This work was also supported by the Istituto Nazionale di Astrofisica (PRIN-INAF-2014), by the University of Catania (PRIN MIUR 2012) and by the Space Weather Italian COmmunity (SWICO) Research Program.

References

Arnaud, J.,Mein, P.,& Rayrole, J.: 1998, in a Crossroads For European Solar and Heliographic Physics, Tenerife, ESA SP-417, 213

Aschwanden, M. J.: 2004, Physics of the Solar Corona, Praxis (Berlin: Chichester and Springer-Verlag)

Benz A.O.: 2008, Living Rev. Solar Phys. 5

Carmichael, H.: 1964, Proc. of the AAS-NASA Symposium - The Physics of Solar Flares, ed. Wilmot N. Hess, Washington, National Aeronautics and Space Administration, Science and Technical Information Division, 451

Chupp E.L., Forrest D.J., Higbie P.R., Suri A.N., Tsai C., Dunphy P.P.: 1973, Nature 241, 333

De Pontieu B., Title A.M., Lemen J.R., Kushner G.D., Akin D.J., Allard B. et al.: 2014, Sol. Phys. 289, 2733

Domingo V., Fleck B., & Poland,A. I.: 1995, Sol. Phys. 162, 1

Fletcher L., Dennis B.R., Hudson H.S., Krucker S., Phillips K., Veronig A., Battaglia M., Bone L., Caspi A., Chen Q., Gallagher P., Grigis P.T., Ji H., Liu W., Milligan R.O., Temmer M.: 2011, Space Sci. Rev. 159, 19

Forbes T. G., & Priest E. R.: 1995, ApJ 446, 377

Golub, L., et al.: 2007, Sol. Phys. 243, 63

Graham D. & Cauzzi G.: 2015, ApJ 807, L22

Guglielmino S.L., Zuccarello F., Romano P., Cristaldi A., Ermolli E., Criscuoli S., Falco M.: 2016, ApJ, in press

Hirayama, T.: 1974, Solar Phys. 34, 323

Jess D. B. et al.: 2010, Sol. Phys. 261, 363

Jiricka, K., Karlicky, M., Kepka, O., & Tlamicha, A. 1993, Sol. Phys., 147, 203

Kopp, R. A., & Pneuman, G. W.: 1976, Sol. Phys. 50, 85

Kosugi, T., et al.: 2007, Sol. Phys. 243, 3

Lemen J. R., Title A. M., Akin D. J., et al.: 2012, Sol. Phys. 275, 17

Lin R. P., Dennis B. R., Hurford G. J., et al.: 2002, Sol. Phys. 210, 3

Pesnell W. D., Thompson B. J., & Chamberlin P. C.: 2012, Sol. Phys. 275, 3

Polito V., Mason H., Del Zanna G.: 2012, 1st Solar Orbiter Summer School

Prochazka O., M. Mathioudakis., Zuccarello F. et al. 2016, in progress
Romano P. & Zuccarello F.: 2011, A&A 535, 1R
Ruiz Cobo, B. & del Toro Iniesta J. C.: 1992, ApJ 398, 375
Scharmer G. B., Bjelksjo K., Korhonen T. K., Lindberg B. & Petterson B.: 2003, Proc. SPIE 4853, 341
Scharmer G. B., Narayan G., Hillberg T. et al.: 2008, ApJ 689, L69
Scherrer P. H., Bogart R. S., Bush R. I., et al.: 1995, Sol. Phys. 162, 129
Scherrer, P.H., Schou J., Bush R.I., et al.: 2012, Sol. Phys. 275, 207
Sturrock, P.A.: 1966, Nature 211, 695
Zuccarello, F., Romano, P., Farnik, F., Karlicky, M., Contarino, L., Battiato, V., Guglielmino, S. L., Comparato, M., Ugarte-Urra, I.: 2009, A&A 493, 629
Zuccarello F., Contarino L. & Romano P.: 2011, CoSka 41, 85